

A segmented conical electric lens for optimization of the beam spot of the low-energy muon facility at PSI: a Geant4 simulation analysis

Ran Xiao^{1,2,3} · Elvezio Morenzoni³ · Zaher Salman³ · Bang-Jiao Ye^{1,2} · Thomas Prokscha³

Received: 27 July 2016/Revised: 19 October 2016/Accepted: 12 November 2016/Published online: 30 January 2017
© Shanghai Institute of Applied Physics, Chinese Academy of Sciences, Chinese Nuclear Society, Science Press China and Springer Science+Business Media Singapore 2017

Abstract The low-energy muon facility at PSI provides nearly fully polarized positive muons with tunable energies in the keV range to carry out muon spin rotation (LE- μ SR) experiments with nanometer depth resolution on thin films, heterostructures, and near-surface regions. The low-energy muon beam is focused and transported to the sample by electrostatic lenses. In order to achieve a minimum beam spot size at the sample position and to enable the steering of the beam in the horizontal and vertical direction, a special electrostatic device has been implemented close to the sample position. It consists of a cylinder at ground potential followed by four conically shaped electrodes, which can be operated at different electric potential. In LE- μ SR experiments, an electric field at the sample along the beam direction can be applied to accelerate/decelerate muons to different energies (0.5–30 keV). Additionally, a horizontal or vertical magnetic field can be superimposed for transverse or longitudinal field μ SR experiments. The focusing properties of the conical lens in the presence of these additional electric and magnetic fields have been investigated and optimized by Geant4 simulations. Some

experimental tests were also performed and show that the simulation well describes the experimental setup.

Keywords Muon beam · Muon spin rotation · Low-energy muon · Beam size · Geant4

1 Introduction

The muon spin rotation/relaxation/resonance (μ SR) technique is a versatile local probe technique to investigate the physical properties of superconductors, magnetic systems, semiconductors, and organic materials [1]. Polarized muon beams for μ SR applications are usually produced at medium energy (0.5–3 GeV) proton accelerators. These muons have kinetic energies of the order of MeV and penetrate deeply into a sample (mm to cm). Therefore, μ SR experiments using these MeV muons can only study bulk materials. To overcome these limitations and to extend μ SR to the investigation of thin films, PSI developed and operates the low-energy muons beam facility (LEM) where a cryogenic moderation method [2–6] is used to generate nearly fully polarized positive muons with tunable energies in the range of eV to several keV. Up to now, the LEM facility at PSI has played a leading role in low-energy muon experiments, extending the μ SR technique to the investigation of nano-materials, layer interfaces, thin films, and near-surface regions [7–19].

The LEM facility is located at the μ E4 beam line, which is a hybrid-type large acceptance channel to generate an intense beam of so-called surface muons (positive muons, μ^+ , originating from pions decaying at rest close to the surface of the pion/muon target with a kinetic energy of ~ 4 MeV) [6]. The intensity of the surface muon beam at

✉ Ran Xiao
xran@mail.ustc.edu.cn

✉ Thomas Prokscha
thomas.prokscha@psi.ch

¹ State Key Laboratory of Particle Detection and Electronics, University of Science and Technology of China, Hefei 230026, China

² Department of Modern Physics, University of Science and Technology of China, Hefei 230026, China

³ Laboratory for Muon Spin Spectroscopy, Paul Scherrer Institut (PSI), 5232 Villigen, Switzerland

Table 1 Simulated optimum values of (RAL-RAR) (Unit: kV) to steer the beam spot to the center at different electric potentials at the sample between -10 and 10 kV, and different AEW magnetic fields from 0 to 300 Gauss, $V_{\text{mod}}=15$ kV

	-10 kV	-5 kV	0	5 kV	10 kV
50 G	-0.36	-0.38	-0.40	-0.50	-0.6
100 G	-0.68	-0.70	-0.76	-0.82	-0.9
150 G	-1.00	-1.10	-1.20	-1.20	-1.2
200 G	-1.25	-1.50	-1.70	-1.60	-1.6
250 G	-1.60	-1.70	-1.85	-2.00	-2.0
300 G	-2.00	-2.10	-2.20	-2.30	-2.4

RAL + RAR = 23.8 kV

the exit of the μE4 beam line is about $4.6 \times 10^8/\text{s}$ at a proton current of 2.2 mA. This represents, at the moment, the highest continuous surface muon flux in the world. About 40% of the beam is focused onto the cryogenic moderator target. Using a wide-band-gap van der Waals solid gas ($s\text{-N}_2$, $s\text{-Ar}$), a moderation efficiency $\left(\frac{N_{\text{eV}}^{\text{out}}}{N_{\text{MeV}}^{\text{in}}}\right)$ between 10^{-5} and 10^{-4} is achieved [2, 4, 8].

The moderation of the muons from about 4 MeV to 10 eV is achieved within 10 ps, such that their initial high polarization is conserved [5]. The moderator consists of a $200\text{--}300\text{-nm}$ -thick Ar layer (capped by a 10-nm -thin N_2 layer) deposited on a thin Ag foil (~ 125 μm) [20] which is held by a cryostat at a temperature below 20 K. The mean energy of the moderated muons is about 15 eV with a width of about 20 eV (full width at half maximum, FWHM) [21]. These moderated muons can be re-accelerated by applying a high positive potential of up to 20 kV to the moderator [22]. After acceleration, they are transported by electro- and magnetostatic beam elements to the sample position. The rate of the moderated muons of the sample is up to $4.5 \times 10^3/\text{s}$.

By tuning the high voltage of the moderator and the acceleration/deceleration high voltage of the sample, low-energy positive muons ($\text{LE-}\mu^+$) with tunable implantation energies between 0.5 and 30 keV are obtained, corresponding to mean implantation depths ranging from a few nanometers to a few hundred nanometers in solid materials [23]. In addition to the electric acceleration/deceleration field of the sample, an external magnetic field—either parallel or perpendicular to the muon momentum—can be applied for transverse and longitudinal field μSR measurements. These fields may influence the beam spot size and position. A special optical element with four conically shaped segments (also called ring anode, RA) is used to focus the beam onto the sample. Its focusing and steering effects in combination with the applied electric and magnetic fields have been investigated using the musrSim

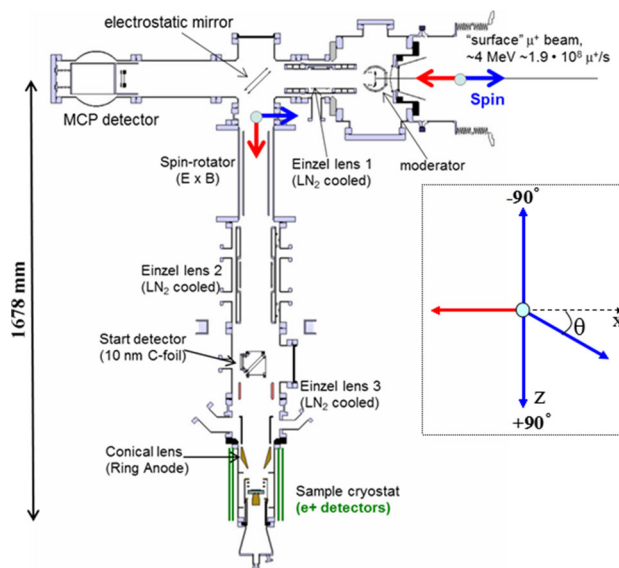


Fig. 1 Layout of the low-energy muon beam line for LE- μSR experiments at PSI. The red and blue arrows in the figure represent the muon's momentum and direction of spin polarization, respectively. θ_{spin} represents the spin angle with respect to the initial direction of the 4-MeV muon beam, corresponding to $-x$ direction in the simulation

simulation package [24] which is based on Geant4 [25, 26]. Using these simulations, we optimize the settings of RA for the various magnetic fields and varying implantation energies (electric fields) and compare them with experimental data. These parameters allow us to run the experiment with optimized beam transport onto the sample under different magnetic and electric field configurations. The results of this analysis are presented in this paper.

2 Setup of the low-energy muon beam

A schematic of the LEM apparatus is shown in Fig. 1. The low-energy muon beam is extracted from the cryogenic moderator with a quadratic area of 30×30 mm^2 . Adjustable positive high voltages applied to the moderator and to a set of grids generate an accelerating electric field to re-accelerate the moderated muons from eV to higher energies, typically between 10 keV and 20 keV (low-energy muons). Only a small fraction of surface muons is moderated to eV energies, and most of the surface muons stop in the moderator target or leave the moderator with keV to hundreds of keV energies (fast muons). An electrostatic mirror with an angle of 45° with respect to the muon momentum is used to separate low-energy from fast muons. After being focused by einzel lens 1 (L1), the low-energy muons are deflected by 90° with respect to the initial muon direction, while the fast ones continue in the direction of the MCP detector. After the deflection, the spin

polarization is perpendicular to the muon momentum. A spin rotator with crossed static magnetic and electric fields $\vec{E} \times \vec{B}$ can be used to rotate the muon spin parallel or antiparallel to its momentum [27]. This enables us to carry out longitudinal field measurements (LF- μ SR, where the muon spin is parallel or antiparallel to the applied field at the sample). The LE- μ^+ spin angle (θ_{spin}) can be changed between -90° and $+90^\circ$ with respect to the initial direction of the 4-MeV muon beam by tuning the magnetic and electric fields in the spin rotator such that the ratio E/B matches the velocity of the muons. Downstream of the spin rotator, the einzel lens 2 (L2) focuses the muon beam onto the retractable start detector. This detector provides the fast start timing signal, which is necessary for μ SR experiments at a continuous muon beam. Its time resolution is about 1 ns, the detection efficiency for keV muons is $\sim 80\%$, and it introduces an increase in transverse phase space due to multiple scattering and an increase in the initial width of the energy distribution of 20 eV FWHM to about 1 keV FWHM. The detector is described in detail in Refs. [29, 30]. The final beam size at the sample position is determined by lens 3 (L3) and the strongly focusing conical lens, RA. It consists of the four segments RAT, RAB, RAL, and RAR; see Fig. 2. These segments are made of gold-plated polished copper and are attached to a grounded stainless steel cylinder by pairs of macor or sapphire insulators. In contrast to an einzel lens, the conical lens can be placed closer to the sample position, thus allowing for stronger focusing and a smaller beam spot. The beam can

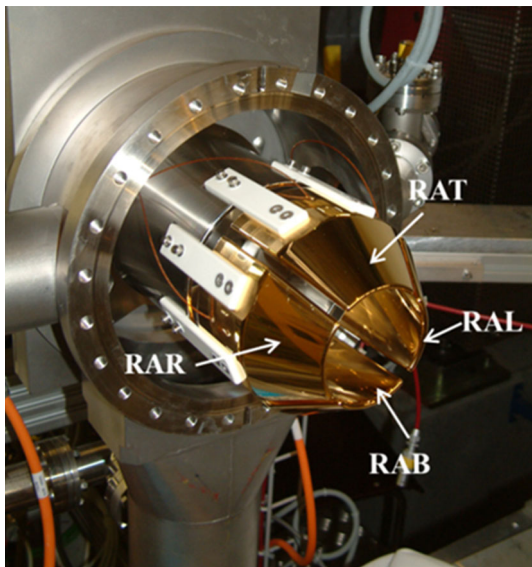


Fig. 2 Four segments of the ring anode RA: the *top* segment RAT, the *bottom* segment RAB, the *right* segment RAR, and the *left* segment RAL, attached to a grounded stainless steel cylinder by pairs of macor insulators. The *left and right* segments of the RA sectors are named with respect to the muon beam direction

be shifted in horizontal and vertical direction by applying potential differences between the segments.

Compared to other low-energy particle beams with millimeter size beam extension and low emittances, the PSI low-energy muon beam has a large phase space due to the large source size of $30 \times 30 \text{ mm}^2$, the initial $\cos \theta$ angular distribution (see Sect. 3), and the additional increase in phase space after passing the beam through the 10-nm-thin carbon foil of the start detector. This makes beam transport with a final small beam spot much more challenging.

3 Optimization of RA focusing with applied external magnetic and electric fields at the sample

In the LEM beam Geant4 simulation, the initial muon beam is started at the moderator located at the edge of the high-voltage acceleration region. The moderator is located at a distance of 499 mm upstream to the center of the electrostatic mirror. We assume homogeneous electric fields in the acceleration volume. In the simulation, we studied the beam transport for various beam energies, i.e., moderator potentials V_{mod} : 10, 12, and 15 kV. The initial beam is homogeneously distributed on the moderator area of $30 \times 30 \text{ mm}^2$, and the initial mean kinetic energy is 15 eV with a FWHM of 20 eV. Due to the homogeneous angular distribution of slow muons inside the moderator, [20] a $\cos \theta$ angular distribution is generated in the simulation for muons escaping from the moderator layer, where θ is the angle of the muon momentum with respect to the initial beam direction (the $-x$ direction in the simulation).

Field maps of the beam elements (Spin Rotator, L1, L2, L3 and RA) have been either calculated or measured [27, 28, 30] and are scaled according to the experimental settings. In the electrostatic mirror, a homogeneous electric field is assumed.

A vertical magnetic field up to 300 Gauss, parallel to the sample surface, is supplied by the AEW magnet for transverse field μ SR measurements (TF- μ SR, muon spin transverse to the applied field), and a magnetic field of up to 3400 Gauss can be applied perpendicular to the sample surface and along the muon beam direction (WEW magnet, LF- or TF- μ SR, depending on the initial muons spin polarization). The AEW magnet consists of air-cooled coils (8 A maximum current) wound around a soft-iron yoke with a magnet gap of 154 mm. Because of this large gap, soft-iron pieces inside the vacuum tube are used to reduce the effective length of the magnet and its fringe field region and to increase the maximum available magnetic field at the sample position. The WEW magnet consists of two water-cooled coils made of square copper hollow conductors (600 A maximum current) in Helmholtz geometry surrounded by a soft-iron housing to reduce the stray fields

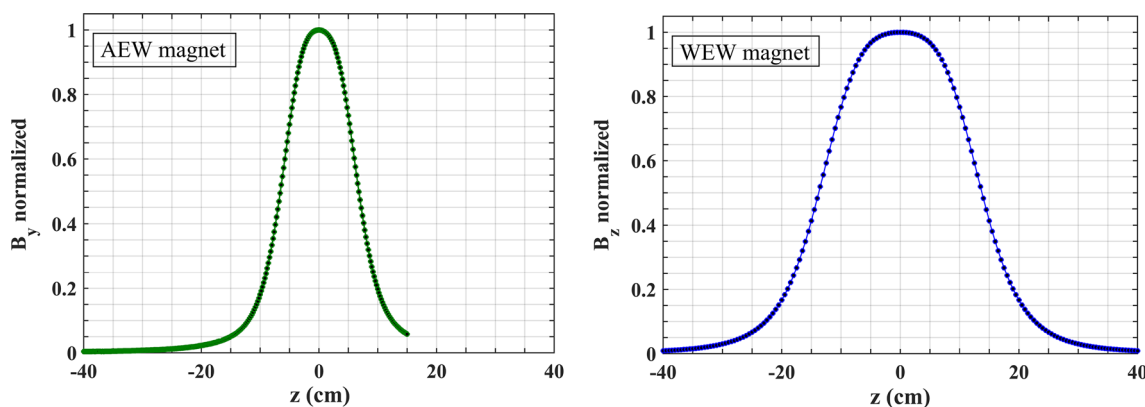


Fig. 3 Normalized magnetic field along beam axis z of the AEW magnet (measured) and WEW magnet (calculated). $z = 0$ corresponds to the sample position

outside of the magnet and to maximize the available field at the sample position. The iron housing of the magnet has a length of 285 mm in beam direction and a front face size of $540 \times 540 \text{ mm}^2$. The magnetic field along the beam axis is shown for both magnets in Fig. 3. The effective lengths of the magnets are 152 mm for the AEW magnet and 295 mm for the WEW magnet.

An acceleration/deceleration high voltage of up to $\pm 12.5 \text{ kV}$ can be applied at the sample plate in order to tune the final implantation energy of the $\text{LE-}\mu^+$.

3.1 Beam spot with vertical magnetic field

3.1.1 Effect of vertical magnetic field on beam spot

In this section, we investigate the effects of the vertical magnetic field (AEW magnet) and of an accelerating/decelerating electric field at the sample on the beam spot for different fields and implantation energies. In addition, we simulate the steering and focusing effects of RA. This allows us to optimize the RA settings for the different magnetic field configurations, which can be used as reference values for the experiment. Figure 4 shows the simulated muon beam spot at the sample position for a muon extraction voltage of $V_{\text{mod}} = 15 \text{ kV}$ without external fields at the sample. The beam spot is well centered in this case, in agreement with the experiment (not shown). Figure 5 shows beam spots without electric field at the sample, viewed from downstream for different AEW magnetic fields: 50, 100, 150, 200, 250, and 300 Gauss. The beam spot shifts almost linearly to the left with increasing magnetic field while the shape of the beam spot is only marginally affected. The mean vertical position remains almost constant. The mean horizontal position (meanX) for different electric fields and vertical magnetic fields is shown in Fig. 6. The absolute value of meanX increases nearly linearly with increasing magnetic field, and the beam spot shift is larger in a

decelerating electric field. In order to keep the beam spot in the center, a potential difference has to be applied between the RAL and RAR segments of RA. Its effect on the beam spot is studied in the next subsection.

3.1.2 Effect of beam steering by RA

The effect of beam steering by applying a potential difference between opposite RA segments is illustrated in Fig. 7 for beam transport with $V_{\text{mod}} = 10 \text{ kV}$, where we compare the experimental and simulated beam spots at the sample. In the experiment, the beam spot at the sample position is measured using a 44-mm-diameter Roentdek

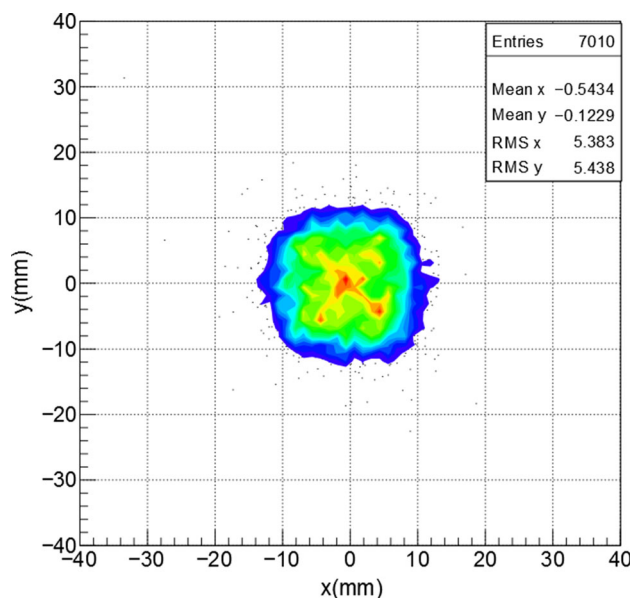


Fig. 4 Simulated beam spot without external fields at the sample position using optimized experimental high-voltage settings for the beam line elements at $V_{\text{mod}} = 15 \text{ kV}$, $\theta_{\text{spin}} = -10^\circ$: L1 = 9.0 kV, L2 = 10.5 kV, L3 = 11.5 kV and RA = 11.9 kV. The initial number of muons at the moderator (N^m) is 10^4

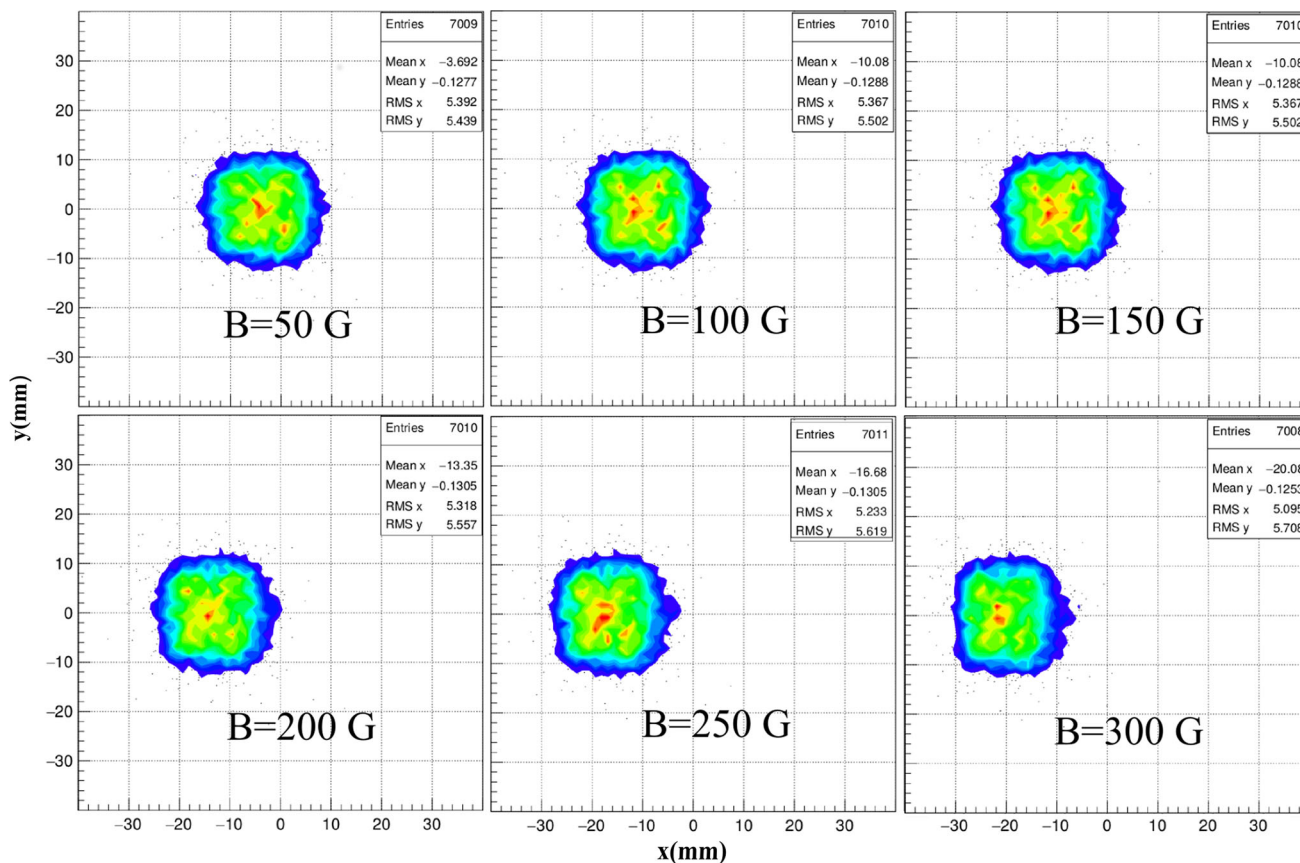


Fig. 5 Simulated beam spots at the sample viewed from downstream in different AEW magnetic fields (50–300 Gauss) with the same beam element settings as shown in Fig. 2

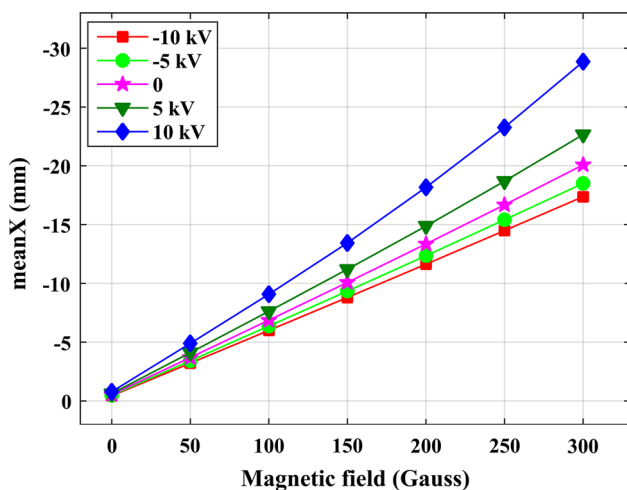


Fig. 6 meanX values with electric potentials at the sample from -10 to 10 kV and AEW magnetic fields from 0 to 300 Gauss ($V_{mod} = 15$ kV)

DLD40 delay line detector with three resistance matched Hamamatsu MCPs in a Z configuration. The top two beam spots of Fig. 7 are for RAL-RAR = -0.64 kV (RAL = 7.18 kV, RAR = 7.82 kV, RAT = RAB = 7.50 kV), where the beam spot center shifts to the left side with meanX = -9.5

mm (in experiment) and -8.4 mm (in simulation). The results for RAL-RAR = 0.56 kV (RAL = 7.78 kV, RAR = 7.22 kV, RAT = RAB = 7.50 kV) are shown in the bottom two figures. In this case, the beam spot shifts to the right side with meanX = 8.8 mm (in experiment) and 7.6 mm (in simulation). The agreement between experiment and simulation is fairly good. The small deviations can be explained by the uncertainty in the applied potentials in the experiment. The used high-voltage power supplies have an absolute uncertainty between 10 and 30 V which results in an overall uncertainty of about 50 V per power supply by taking into account additional uncertainties in the analog control of the power supplies. The beam spot is deformed to a trapezoidal shape, which is different from the effect of the magnetic field which does not cause a deformation. This deformation is caused by lens aberrations in the RA due to proximity of the beam to the electrodes and the broken fourfold symmetry of the electric field in case of a potential difference applied between two opposite segments. In the simulation, the transmission from the moderator to the sample at 10 kV is about 55%, compared to about 70% at 15 kV, where we define the transmission as $\frac{N^{out}}{N^{in}} \times 100\%$, with N^{out} the number of muons in the sample plane, and N^{in} the

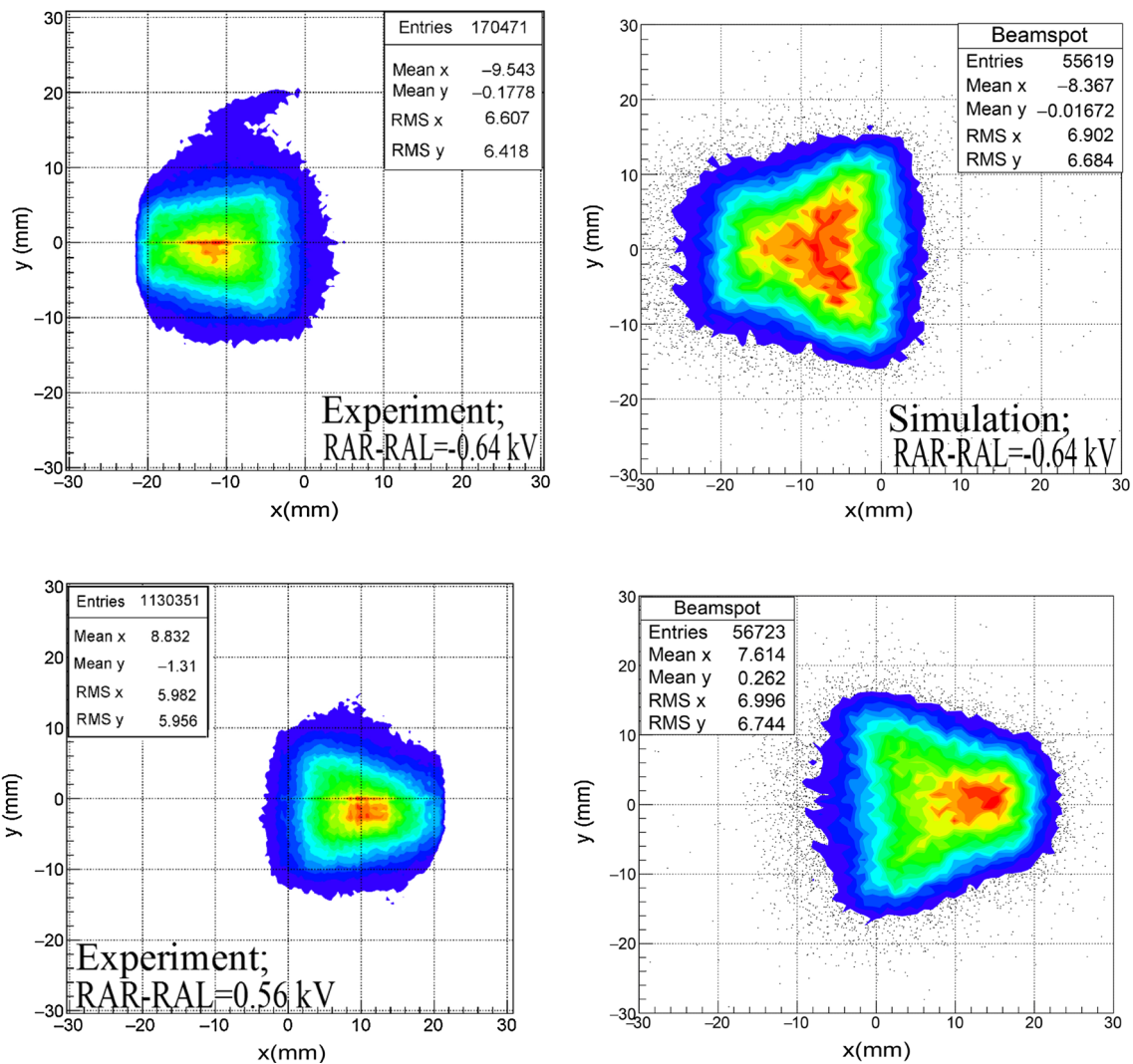


Fig. 7 Comparison of measured and simulated beam spots at the sample viewed from upstream with $RAT = RAB$, $RAL-RAR = -0.64$ kV (top), and 0.56 kV (bottom). Other parameters are: $V_{mod}=10.0$ kV,

$L1 = 6.0$ kV, $L2 = 7.0$ kV, $L3 = 8.0$ kV, $RAT = RAB = 7.5$ kV, and $\theta_{spin} = -10^\circ$. The initial number of muons at the moderator in the simulation is 10^5

initial number of muons at the moderator. The reduction in the transmission is due to (1) a longer time of flight at 10 kV, which increases the fraction of muons decaying in flight by about 5% at 10 kV compared to 15 kV, (2) a 10% higher muonium formation (bound neutral state of a μ^+ and an e^-) probability in the 10-nm-thin carbon foil of the start detector, and (3) larger beam divergence at 10 kV after the start detector. In the experiment, we observe a corresponding drop of event rate when changing the beam transport settings from 15 to 10 kV.

3.1.3 Centering of the beam spot at the sample by RA steering

A potential difference between the RAL and RAR segments allows us to counteract the action of the AEW

magnetic field and to steer the beam spot back to the center at the sample position. For muons extracted with 15 kV at the moderator and whose beam spot shifts are shown in Fig. 5, the optimum potential differences obtained by the simulation are shown in Table 1 for different sample potentials (i.e., implantation energies) and AEW magnetic fields. The other transport element parameters in the simulation are the same as those given in Fig. 4.

Figure 8 shows the simulated beam spots after centering by using the RA parameters given in Table 1. The shape of the beam spot is deformed with increasing $|RAL-RAR|$ to a trapezoid instead of the initial square. When $|RAL-RAR| > 2$ kV the beam spot splits into two parts, the larger one keeping the previous trapezoidal shape and the smaller one having an ellipsoidal shape.

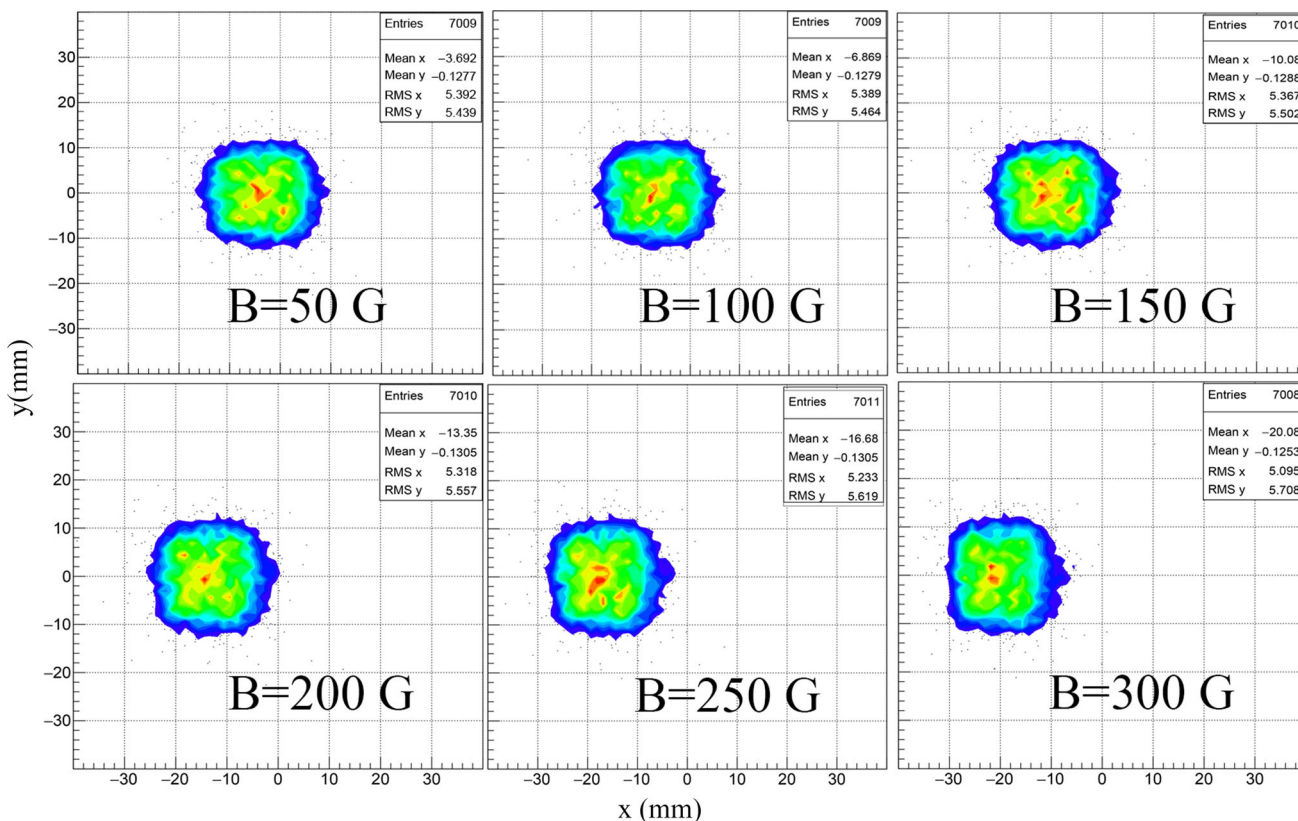


Fig. 8 Simulated beam spots at the sample position viewed from downstream with the maximized number of muons in the center. The centering of the beam spot is obtained by using the RA potential differences given in Table 1. Vertical magnetic field (AEW magnet)

varies from 50 to 300 Gauss with the same beam element settings as shown in Fig. 4 ($V_{mod}=15$ kV, $RA = 11.9$ kV). Pictures from *left to right* and *top to bottom* are the beam spots with different AEW magnetic fields (50 to 300 Gauss) at the sample with zero sample bias

Table 2 Fraction η of muons stopping in an area of 20×20 mm² in the center of the beam spot after steering by RA according to Table 1 for different electric and AEW magnetic fields, $V_{mod} = 15$ kV

	-10 kV	-5 kV	0 kV	5 kV	10 kV
0	93.7	93.2	91.9	90.4	87.6
50 G	93.3	92.7	91.7	89.0	86.2
100 G	91.7	91.3	88.8	86.2	81.1
150 G	88.6	85.4	81.4	73.2	64.3
200 G	84.0	85.0	74.1	69.4	63.2
250 G	80.5	79.6	76.9	66.4	56.5
300 G	79.4	75.2	68.9	62.4	62.1

(Unit:%)

This splitting causes the meanX value to deviate from zero while the muon rate in the center of the sample plane is maximized.

The fraction $\eta = N_{[-10,10]mm}^{out} / N^{out}$ of muons stopping in an area of $x, y \in [-10, 10]$ mm in the center of the beam spot is shown in Table 2 after RA steering. Before adjusting RA, this fraction is smaller than 10% when a 300-Gauss magnetic field is applied, and it further reduces to

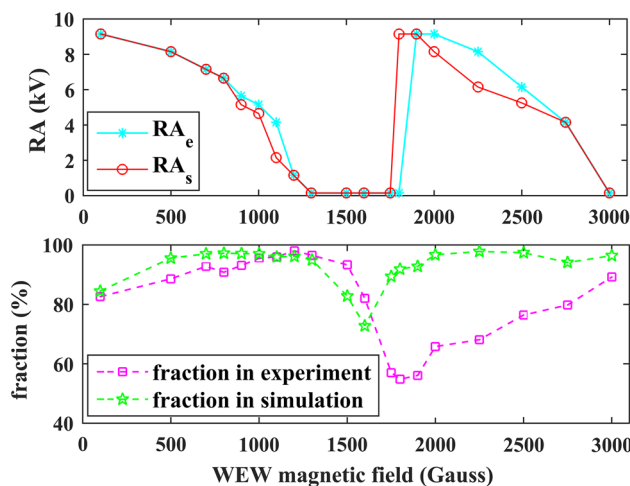


Fig. 9 Optimized RA potential values (*top*) and the corresponding fractions (*bottom*) of the beam stopping in the central area of 20×20 mm² at the sample for different WEW magnetic fields for a moderator potential of 12 kV. RA_e and RA_s are the best values in the experiments and simulations, respectively

less than 1% when a positive bias of +5 and +10 kV is applied at the sample. After steering, most of the muons ($> 60\%$) are shifted to the 20×20 mm² area in the center.

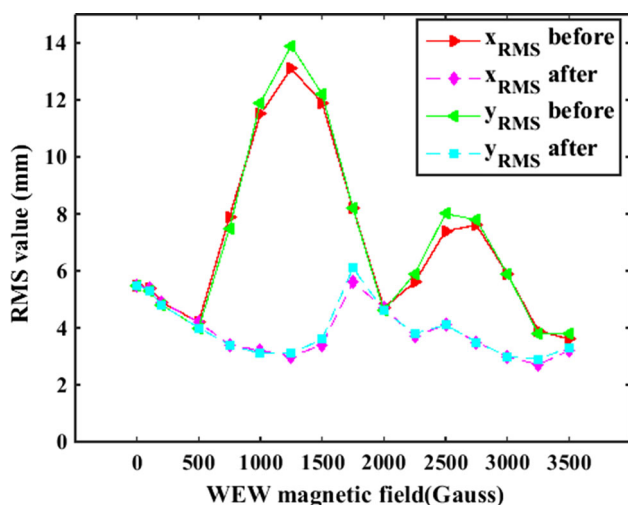


Fig. 10 x_{RMS} and y_{RMS} of the muon beam spot at the sample at different WEW magnetic fields before and after tuning RA with $V_{mod} = 15$ kV. Data labeled “before” and “after” are for RA = 11.9 kV for all magnetic fields before optimizing RA in the simulation and after setting the RA according to the values in Table 3, respectively

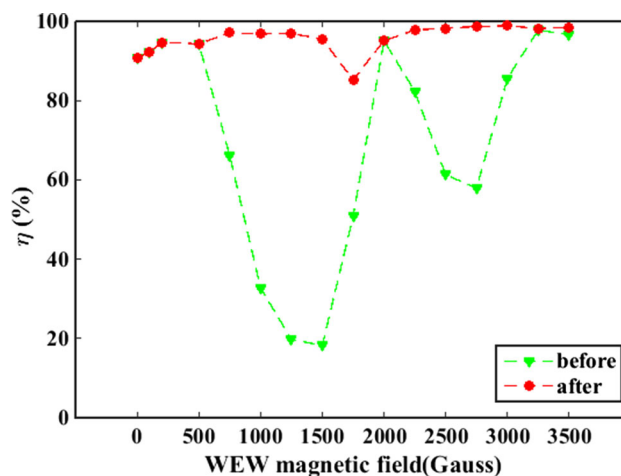


Fig. 11 Fraction, η , of muons stopping in the central area of 20×20 mm² at the sample position with different WEW magnetic fields parallel to the muon before and after optimizing RA with $V_{mod} = 15$ kV. Data labeled “before” and “after” are for RA = 11.9 kV for all magnetic fields before optimizing RA in the simulation and after tuning RA according to Table 3, respectively

3.2 Beam spot with horizontal magnetic field

In this section, we investigate the effects of a horizontal magnetic field parallel to the beam axis on the beam spot for different fields and implantation energies. This magnetic field at the sample is generated by the WEW magnet for LF- and TF- μ SR experiments. The muon beam spot at the sample may be influenced by the WEW magnetic field by field components perpendicular to the muon momentum. An experimental determination of the optimal RA settings is obtained by maximizing the fraction, η , of muons landing within an area of 20×20 mm² at the sample position. This can be done by measuring the TF- μ SR precession amplitude on a 20×20 mm² gold foil glued onto a Ni-coated large plate. Muons stopping in the gold foil maintain their polarization and hence contribute to the measured signal while muons landing in the Ni backing depolarize almost immediately and do not contribute to the precession amplitude. Measurements of the precession amplitude as a function of RA voltage were performed using the positron detectors, with $V_{mod} = 12$ kV. Figure 9 shows good agreement between experimental (RA_e) and simulated (RA_s) optimum RA values for WEW fields up to 1600 Gauss. At higher fields, there are differences up to

about 2500 Gauss, where the RA_s values deviate by one to two kV from the experimental RA_e optimum settings. At even higher fields, RA_e and RA_s agree again up to the maximum measured field of 3000 Gauss. We attribute the discrepancies to a slightly off-centered beam in the experiment and possible differences between the calculated WEW field map used in the simulation and the actual experimental one. The off-centered beam is caused by a slightly tilted muon moderator target and possible misalignment of optical elements, which in turn introduces additional transverse velocity components in the beam, causing a shift and off-centered beam spot as a function of magnetic field. This affects the fraction of muons stopping in the central area of 20×20 mm².

The RMS values of simulated beam spots at different WEW magnetic field from 0–3500 Gauss at $V_{mod} = 15$ kV are displayed in Fig. 10. For RA fixed at 11.9 kV, the beam size significantly increases between 500 Gauss and about 2000 Gauss due to the varying focusing power of the magnet. This can be corrected by lowering the RA potential to reduce the focusing power of RA. As in the case of the $V_{mod} = 12$ kV data, the RA potential was tuned to maximize the fraction η of muons stopping in the central area of 20×20 mm² of the sample plane. Table 3

Table 3 Optimized RA potential values for different WEW magnetic fields, $V_{mod} = 15$ kV

B (Gauss)	100	200	500	750	1000	1250	1500	1750	2000	2250	2500	2750	3000	3250	3500
RA (kV)	11.9	11.9	11.9	10.0	7.6	3.8	0	0	11.2	10.5	7.2	4.2	0.0	0.0	11.0

summarizes these optimized RA potential values to achieve the smallest beam spot size at the sample. One can see that the RA voltage can be kept constant up to 500 Gauss before it has to be lowered to compensate for the increasing focusing power of the magnet. At some magnetic fields (such as $B = 1500, 1700$ Gauss), there is no need to use the RA to focus the beam ($RA = 0$). Compared to the $V_{\text{mod}} = 12$ kV data, the RA has to be turned on again to obtain the smallest beam spot at a field of about 2000 G, which is higher than the ~ 1750 G at $V_{\text{mod}} = 12$ kV. This shift is expected due to the $\sqrt{15 \text{ keV}/12 \text{ keV}}$ higher momentum of the muon beam; at higher beam momentum one needs a correspondingly higher magnetic field to obtain the same beam transport properties of the WEW magnetic field. Figure 11 compares the fraction, η , at the sample before and after tuning the RA at different WEW magnetic fields. It is obvious that η can be significantly increased by proper tuning of RA. The fractions η at $V_{\text{mod}} = 15$ kV are higher than at $V_{\text{mod}} = 12$ kV because of the smaller increase in transverse phase space when passing through the carbon foil of the start detector; the mean scattering angle due to multiple scattering is lower at higher beam energy.

4 Summary

In this paper, we presented the focusing and steering properties of a segmented conical electrostatic lens (RA), which serves as a lens with large focusing power for the keV muon beam of the LE- μ^+ facility at PSI. This beam optics element is essential for obtaining a small beam spot in the very limited space available in the sample region of the LE- μ SR setup. We presented a detailed Geant4 investigation of the beam transport to optimize the experimental conditions for the present LEM setup, where we studied the beam transport onto the sample plane in the presence of various magnetic and electric fields in the sample region. In some cases, the availability of experimental data allowed comparing the simulation with the experimental data. Good agreement is found, which demonstrates that the optical properties of RA are well described in the simulation. Using the simulation, we optimized the electric potential settings of RA in the case of a vertical magnetic field at the sample position. This field is transverse to the muon momentum and requires steering by RA to center the beam spot. In the case of a magnetic field along the beam direction, the increasing focusing power of the magnet has to be compensated by a reduction in the RA focusing power. The simulation can be used to optimize RA for various experimental conditions in the sample region without the need of running an experiment to test the beam properties at the sample position for each case. This is

important for the design and analysis of future LE- μ SR experiments. A long-term goal is the reduction in the beam spot size to allow the investigation of standard $5 \times 5 \text{ mm}^2$ samples. At present, the study of such samples is only possible by using a mosaic of at least four pieces of this size. In many cases, it is not possible to generate four or more identical samples which makes some experiments unfeasible. To achieve this long-term goal, the understanding and the reliability of the simulation of the used optical beam elements are essential, especially the design of the last focusing element where the present work provides important information. Finally, we emphasize that Geant4 simulations are very powerful to describe and optimize experimental setups and to help push experimental capabilities to their limit.

Acknowledgements Ran Xiao acknowledges a scholarship from the China Scholarship Council (CSC) and financial support from PSI for her stay at PSI.

References

1. A. Yaouanc, P.D. de Réotier, *Muon Spin Rotation, Relaxation, and Resonance: Applications to Condensed Matter* (Oxford University Press, Oxford, 2011)
2. E. Morenzoni, Physics and applications of low energy muons, *Muon Science: Muons in Physics, Chemistry and Materials* (Bristol and Philadelphia, 1999), vol. 51, eds. by S.L. Lee, S.H. Kilcoyne, R. Cywinski, pp. 343–404 (1998)
3. E. Morenzoni, H. Glückler, T. Prokscha et al., Low-energy μ SR at PSI: present and future. *Phys. B: Condens. Matter* **289**, 653–657 (2000). doi:[10.1016/S0921-4526\(00\)00303-3](https://doi.org/10.1016/S0921-4526(00)00303-3)
4. D. Harshman Jr., A. Mills, J. Beveridge et al., Generation of slow positive muons from solid rare-gas moderators. *Phys. Rev. B* **36**, 8850 (1987). doi:[10.1103/PhysRevB.36.8850](https://doi.org/10.1103/PhysRevB.36.8850)
5. E. Morenzoni, F. Kottmann, D. Maden et al., Generation of very slow polarized positive muons. *Phys. Rev. Lett.* **72**, 2793 (1994). doi:[10.1103/PhysRevLett.72.2793](https://doi.org/10.1103/PhysRevLett.72.2793)
6. T. Prokscha, E. Morenzoni, K. Deiters et al., The new $\mu e4$ beam at PSI: a hybrid-type large acceptance channel for the generation of a high intensity surface-muon beam. *Nucl. Instrum. Methods A* **595**, 317–331 (2008). doi:[10.1016/j.nima.2008.07.081](https://doi.org/10.1016/j.nima.2008.07.081)
7. E. Morenzoni, R. Khasanov, H. Luetkens et al., Low energy muons as probes of thin films and near surface regions. *Phys. B: Condens. Matter* **326**, 196–204 (2003). doi:[10.1016/S0921-4526\(02\)01601-0](https://doi.org/10.1016/S0921-4526(02)01601-0)
8. E. Morenzoni, T. Prokscha, A. Suter et al., Nano-scale thin film investigations with slow polarized muons. *J. Phys.: Condens. Matter* **16**, S4583 (2004). doi:[10.1088/0953-8984/16/40/010](https://doi.org/10.1088/0953-8984/16/40/010)
9. T. Prokscha, K. Chow, E. Stilp et al., Photo-induced persistent inversion of germanium in a 200-nm-deep surface region. *Sci. Rep.* **3**, 2569 (2013). doi:[10.1038/srep02569](https://doi.org/10.1038/srep02569)
10. E. Morenzoni, T. Prokscha, H. Saadaoui, et al., Low-energy muons at PSI: examples of investigations of superconducting properties in near-surface regions and heterostructures, in *Proceedings of the International Symposium on Science Explored by Ultra Slow Muon (USM2013)*, *JPS Conference Proceedings*, Vol. 2, id. 010201, p. 10, , p. 0201, 2014. doi:[10.7566/JPSCP.2.010201](https://doi.org/10.7566/JPSCP.2.010201)

11. L. Schulz, L. Nuccio, M. Willis et al., Engineering spin propagation across a hybrid organic/inorganic interface using a polar layer. *Nat. Mater.* **10**, 39–44 (2011). doi:[10.1038/nmat2912](https://doi.org/10.1038/nmat2912)
12. A. Suter, E. Morenzoni, T. Prokscha et al., Two-dimensional magnetic and superconducting phases in metal-insulator $\text{La}_{2-x}\text{Sr}_x\text{CuO}_4$ superlattices measured by muon-spin rotation. *Phys. Rev. Lett.* **106**, 237003 (2011). doi:[10.1103/PhysRevLett.106.237003](https://doi.org/10.1103/PhysRevLett.106.237003)
13. A. Boris, Y. Matiks, E. Benckiser et al., Dimensionality control of electronic phase transitions in nickel-oxide superlattices. *Science* **332**, 937–940 (2011). doi:[10.1126/science.1202647](https://doi.org/10.1126/science.1202647)
14. A. Hofmann, Z. Salman, M. Mannini et al., Depth-dependent spin dynamics in thin films of TbPc_2 nanomagnets explored by low-energy implanted muons. *ACS Nano*. **6**, 8390–8396 (2012). doi:[10.1021/nm3031673](https://doi.org/10.1021/nm3031673)
15. E. Stilp, A. Suter, T. Prokscha et al., Controlling the near-surface superfluid density in underdoped $\text{YBa}_2\text{Cu}_3\text{O}_{6+x}$ by photo-illumination. *Sci. Rep.* **4**, 6250 (2014). doi:[10.1038/srep06250](https://doi.org/10.1038/srep06250)
16. H. Saadaoui, Z. Salman, H. Luetkens et al., The phase diagram of electron-doped $\text{La}_{2-x}\text{Ce}_x\text{CuO}_{4-\delta}$. *Nat. Commun.* **6**, 6041 (2015). doi:[10.1038/ncomms7041](https://doi.org/10.1038/ncomms7041)
17. F. Al Ma'Mari, T. Moorsom, G. Teobaldi et al., Beating the stoner criterion using molecular interfaces. *Nature* **524**, 69–73 (2015). doi:[10.1038/nature14621](https://doi.org/10.1038/nature14621)
18. L. Anghinolfi, H. Luetkens, J. Perron et al., Thermodynamic phase transitions in a frustrated magnetic metamaterial. *Nat. Commun.* **6**, 8278 (2015). doi:[10.1038/ncomms9278](https://doi.org/10.1038/ncomms9278)
19. M. Flokstra, N. Satchell, J. Kim et al., Remotely induced magnetism in a normal metal using a superconducting spin-valve. *Nat. Phys.* **12**, 57–61 (2016). doi:[10.1038/nphys3486](https://doi.org/10.1038/nphys3486)
20. T. Prokscha, E. Morenzoni, C. David et al., Moderator gratings for the generation of epithermal positive muons. *Appl. Surf. Sci.* **172**, 235–244 (2001). doi:[10.1016/S0169-4332\(00\)00857-6](https://doi.org/10.1016/S0169-4332(00)00857-6)
21. P. Bakule, E. Morenzoni, Generation and applications of slow polarized muons. *Contemp. Phys.* **45**, 203–225 (2004). doi:[10.1080/00107510410001676803](https://doi.org/10.1080/00107510410001676803)
22. Low energy muons: overview of the experimental setup. <http://www.psi.ch/low-energy-muons/experimental-setup>
23. E. Morenzoni, H. Glückler, T. Prokscha et al., Implantation studies of keV positive muons in thin metallic layers. *Nucl. Instrum. Methods B* **192**, 254–266 (2002). doi:[10.1016/S0168-583X\(01\)01166-1](https://doi.org/10.1016/S0168-583X(01)01166-1)
24. K. Sedlak, R. Scheuermann, T. Shiroka et al., MusrSim and MusrSimAna-simulation tools for μSR instruments. *Phys. Proced.* **30**, 61–64 (2012). doi:[10.1016/j.phpro.2012.04.040](https://doi.org/10.1016/j.phpro.2012.04.040)
25. S. Agostinelli, J. Allison, K. Amako et al., Geant4—a simulation toolkit. *Nucl. Instrum. Methods A* **506**, 250–303 (2003). doi:[10.1016/S0168-9002\(03\)01368-8](https://doi.org/10.1016/S0168-9002(03)01368-8)
26. J. Allison, K. Amako, J. Apostolakis et al., Geant4 developments and applications. *Nucl. Sci.* **53**, 270–278 (2006). doi:[10.1109/TNS.2006.869826](https://doi.org/10.1109/TNS.2006.869826)
27. Z. Salman, T. Prokscha, P. Keller et al., Design and simulation of a spin rotator for longitudinal field measurements in the low energy muons spectrometer. *Phys. Proced.* **30**, 55–60 (2012). doi:[10.1016/j.phpro.2012.04.039](https://doi.org/10.1016/j.phpro.2012.04.039)
28. T.K. Paraiso, E. Morenzoni, T. Prokscha et al., Geant4 simulation of low energy μSR experiments at PSI. *Phys. B: Condens. Matter* **374**, 498–501 (2006). doi:[10.1016/j.physb.2005.11.140](https://doi.org/10.1016/j.physb.2005.11.140)
29. E. Morenzoni, M. Birke, H. Glückler et al., Generation of very slow polarized muons by moderation. *Hyperfine Interact.* **106**, 229–235 (1997). doi:[10.1023/A:1012610528798](https://doi.org/10.1023/A:1012610528798)
30. K.S. Khaw, A. Antognini, P. Crivelli et al., Geant4 simulation of the PSI LEM beam line: energy loss and muonium formation in thin foils and the impact of unmoderated muons on the μSR spectrometer. *J. Instrum.* **10**, 10025 (2015). doi:[10.1088/1748-0221/10/10/P10025](https://doi.org/10.1088/1748-0221/10/10/P10025)